Nanoscale

ROYAL SOCIETY OF CHEMISTRY

PAPER

View Article Online
View Journal | View Issue

Cite this: *Nanoscale*, 2020, **12**, 14903

Electroactivation-induced IrNi nanoparticles under different pH conditions for neutral water oxidation†

Woong Hee Lee,‡[a] Jaekyung Yi,‡[a,b] Hong Nhan Nong,[c] Peter Strasser,[c] Keun Hwa Chae,[d] Byoung Koun Min,[a,e] Yun Jeong Hwang *[a,b,f] and Hyung-Suk Oh *[a,b]

Electrochemical oxidation processes can affect the electronic structure and activate the catalytic performance of precious-metal and transition-metal based catalysts for the oxygen evolution reaction (OER). Also there are emerging requirements to develop OER electrocatalysts under various pH conditions in order to couple with different reduction reactions. Herein, we studied the effect of pH on the electroactivation of IrNi alloy nanoparticles supported on carbon (IrNi/C) and evaluated the electrocatalytic activities of the activated $IrNiO_x$/C for water oxidation under neutral conditions. In addition, their electronic structures and atomic arrangement were analyzed by *in situ*/*operando* X-ray absorption spectroscopy (XAS) and identical location transmission electron microscopy techniques, showing the reconstruction of the metal elements during electroactivation due to their different stabilities depending on the electrolyte pH. $IrNiO_x$/C activated under neutral pH conditions showed a mildly oxidized thin IrO_x shell. Meanwhile, $IrNiO_x$/C activated in acidic and alkaline electrolytes showed Ni-leached IrO_x and Ni-rich $IrNiO_x$ surfaces, respectively. Particularly, the surface of $IrNiO_x$/C activated under alkaline conditions shows IrO_x with a high d-band hole and NiO_x with a high oxidation state leading to excellent OER catalytic activity in neutral media (η = 384 mV at 10 mA cm^{-2}) whereas much lower OER activity was reported under alkaline or acid conditions. Our results, which showed that electrochemically activated catalysts under different pH conditions exhibit a unique electronic structure by modifying the initial alloy catalyst, can be applied for the design of catalysts suitable for various electrochemical reactions.

Received 14th April 2020,
Accepted 10th June 2020

DOI: 10.1039/d0nr02951c

rsc.li/nanoscale

1. Introduction

Because of the extensive combination of the oxidative half reaction for water splitting, the nitrogen reduction reaction and the carbon dioxide reduction reaction (CO_2RR), the oxygen evolution reaction (OER) is an important step in the path toward developing a sustainable-energy-dependent and clean society.[1–3] For instance, electrochemical water splitting has great significance in providing hydrogen, which is a key chemical fuel in regenerative energy cycles. Moreover, recently, the electrochemical conversion of CO_2 to valuable chemicals has been considered as a promising technology to reduce greenhouse gases and create a clean hydrocarbon energy cycle simultaneously.[4–6] Due to the low amount of CO_2 gas molecules present in alkaline media or overwhelming hydrogen evolution reaction (HER) activity in acidic media, the CO_2RR was typically conducted in neutral pH media such as a buffered bicarbonate electrolyte, which is not a popular condition for water splitting, and the reaction mechanism also varies depending on the pH of the electrolyte. The OER is a bottleneck reaction owing to the sluggish kinetics for the O–H destruction and the O=O bond formation, leading to a high overpotential under neutral conditions as well.[7–9] Therefore, considerable efforts have been focused on finding highly active

[a]*Clean Energy Research Center, Korea Institute of Science and Technology (KIST), Hwarang-ro 14-gil 5, Seongbuk-gu, Seoul 02792, Republic of Korea. E-mail: yjhwang@kist.re.kr, hyung-suk.oh@kist.re.kr; Tel: +82 (0)2 952 5292*
[b]*Division of Energy and Environmental Technology, KIST school, Korea University of Science and Technology, Seoul 02792, Republic of Korea*
[c]*The Electrochemical Energy, Catalysis, and Materials Science Laboratory, Department of Chemistry, Chemical Engineering Division, Technical University Berlin, Berlin 10623, Germany*
[d]*Advanced Analysis Center, Korea Institute of Science and Technology (KIST), Hwarang-ro 14-gil 5, Seongbuk-gu, Seoul 02792, Republic of Korea*
[e]*Green School, Korea University, 145 Anam-ro, Seongbuk-gu, Seoul 02841, Republic of Korea*
[f]*Department of Chemical and Biomolecular Engineering, Yonsei-KIST Convergence Research Institute, Yonsei University, Seoul 03722, Republic of Korea*

†Electronic supplementary information (ESI) available. See DOI: 10.1039/d0nr02951c

‡The authors have contributed equally to this work.

OER catalysts in neutral media with different pH values to minimize the overpotential and increase the energy efficiency.

In recent research, it has been emphasized that not only materials, but also electronic structures have been recently reported to have a strong influence on the catalytic activity for the OER by analyzing the surface states of the electrocatalysts. Even for Ir oxide, one of the best materials for the OER, major efforts have been devoted to transform its electrical structure to enhance its OER activity further.[10–15] Heat treatment is a general method to produce metal oxides. However, rutile IrO_2 synthesized by thermal treatment has a lower OER activity than amorphous IrO_x, which is derived by electrochemical treatment.[16] Jones *et al.* studied the electronic structure of these two different Ir oxides by X-ray photoemission spectroscopy (XPS).[17] Rutile IrO_2 is a composite of Ir^{VI} and O^{II-} species, whereas amorphous IrO_x additionally possesses Ir^{III} and O^{I-} species. Notably, O^{I-} which is considered as an electrophilic oxygen is suitable for the nucleophilic attack of oxygen in water.[18] These O^{I-} species in the IrO_x lattice can participate in water oxidation, leading to enhanced OER catalytic activity.[19,20] Therefore, electrophilic oxygen (O^{I-} species) should be introduced to improve the OER catalytic activity of Ir-based catalysts under neutral conditions.

Recently, alloys of Ir with other metals have been reported in efforts to improve the electrophilic oxidation properties of Ir oxides.[21–30] To activate IrM alloy catalysts, electrochemical treatment was conducted in an acid electrolyte to leach out the non-noble metal components. The surface of the IrM alloy was converted to amorphous IrO_x with increased d-band holes, resulting in the metal-leached IrM@IrO_x metal oxide core–shell catalyst with abundant electrophilic oxygen. Jaramillo *et al.* reported an IrO_x/$SrIrO_3$ catalyst showing excellent OER activity with high durability.[31] Sr is leached out during the initial electrochemical testing, leading to a highly active IrO_x surface layer. Strasser *et al.* demonstrated nickel-leached IrNi@IrO_x nanoparticles with a large number of d-band holes in the IrO_x shell.[32] It has been observed using *operando* X-ray absorption spectroscopy (XAS) that the Ni leached IrO_x shell possesses a massive number of vacancies under oxygen evolution. This leads to the enhanced electrophilic character of oxygen in the catalyst, thus reducing the kinetic barriers for the OER. However, the alloyed metal can have a different chemical stability depending on the environmental conditions such as electrolyte, cation/anion conditions and potential, and the formation of an active layer would be affected by the electrolyte conditions. It has been reported that the unique electronic properties of the catalyst can be obtained by electrochemical treatment at different pH values.[33–35]

In this work, we have studied the effect of the electrochemical activation of IrNi nanoparticles at different pH values to improve the catalytic activity of the OER under neutral conditions. A carbon supported IrNi alloy nanocatalyst (denoted as IrNi/C) was synthesized by a modified polyol process. Electrochemical activations were carried out on IrNi/C by cyclic voltammetry (CV) under acidic, neutral, and alkaline conditions, which are denoted as $IrNiO_x$/C–A, $IrNiO_x$/C–N, and $IrNiO_x$/C–Al, respectively. Changes in the electrocatalyst morphology before and after electrochemical activations were analyzed using identical location transmission electron microscopy (IL-TEM) and IL-HAADF-STEM elemental mapping analysis. $IrNiO_x$/C–A exhibits a nickel-leached IrNi@IrO_x structure, as reported previously.[32] $IrNiO_x$/C–Al shows a nickel-rich $IrNiO_x$ shell structure, while $IrNiO_x$/C–N exhibits a softly oxidized nickel leached Ir oxide shell. $IrNiO_x$/C–Al shows a highly improved OER catalytic activity in neutral media, and the cause of this result was identified by *ex situ* XPS and *in situ*/*operando* XAS measurements.

2. Experimental section

2.1. Synthesis of IrNi bimetallic alloy nanoparticles on carbon black

An IrNi bimetallic nanoparticle alloy supported on carbon black (IrNi/C) was synthesized using oleic acid and oleylamine.[25] A total of 0.45 mmol of nickel acetate tetrahydrate (Sigma-Aldrich), 0.675 mL of oleic acid (Sigma-Aldrich, 70%), and 0.675 mL of oleylamine (Sigma-Aldrich) in 45 mL of dibenzyl ether (Sigma-Aldrich) were added to the reaction flask. The mixture was sonicated to produce a homogeneous solution. The solution was then stirred for 1 h under a nitrogen atmosphere at room temperature. Then, the mixture was heated to 80 °C and maintained at the same temperature for 30 min under a N_2 atmosphere. Iridium acetate (60 mg) and 1,2-dichlorobenzene (5 mL) were added to the reaction mixture. The mixture was then heated to 240 °C for 1 h and subsequently cooled to room temperature. After this process, the mixture was dispersed in 10 mL of dichloromethane and 60 mL of absolute ethanol by adding to it a dispersion of 135 mg of carbon black (Ketjenblack EC 300J) in 30 mL of toluene. The resulting solution was stirred for 1 day at room temperature. The products were collected *via* centrifugation at 6000 rpm and then redispersed in absolute ethanol (Samchun, 100%). This rinsing process was then repeated three times. The resulting powder was dried under ambient conditions for several hours. For the thermal treatment of IrNi/C catalysts, the IrNi/C samples were annealed at 400 °C under 400 cc min^{-1} of N_2 flow and 100 cc min^{-1} of H_2 flow for 4 h.

2.2. Electrochemical measurements

All the electrochemical tests were performed using a rotating disk electrode system (RDE, Pine Research instrument) and a potentiostat VSP (biologic) with a Pt wire as the counter electrode. Hg/Hg_2SO_4 (sat. K_2SO_4, acid, and neutral media) and Hg/HgO (1 M NaOH, alkaline media) were used as reference electrodes. Before the OER test, the electrochemical activation process was conducted by 50 cycles of cyclic voltammetry, between 0.05 and 1.5 V *vs.* RHE at a scan rate of 500 mV s^{-1} in acidic (0.05 M H_2SO_4 purged with N_2), neutral (0.5 M $KHCO_3$ purged with CO_2) and alkaline media (0.1 M KOH purged with N_2). The OER performance was measured in a CO_2-saturated 0.5 M $KHCO_3$ (99.7%, Sigma-Aldrich) aqueous solution (pH

7.4). For the working electrode, ink was prepared by homogeneously suspending 5 mg of the catalysts, 2.49 mL of isopropyl alcohol (Samchun, 99.5%), 2.49 mL of DI water, and 20 μL of 5 wt% Nafion solution (Sigma Aldrich). The synthesized inks were added dropwise onto a glassy carbon electrode (RDE tip, 0.196 cm^2) using a micropipette. The total Ir loading on the RDE was fixed at 20.5 μg cm^{-2}.

2.3. Material characterization

For material characterization, an X-ray diffractometer (XRD, Malvern Panalytical, Empyrean) was used to identify the crystal phases of the synthesized catalysts. X-ray photoelectron spectroscopy (XPS, ULVAC PHI, VersaProbe PHI 5000) and X-ray absorption spectroscopy (XAS) were performed to analyze the oxidation state of the catalysts. For XPS analysis, the catalyst was loaded on carbon paper (SIGACET® GDL, 39 BC) by the spray-coating method. The electrode area was 1 cm^2 and the iridium loading amount was 0.2 mg cm^{-2}. After the electrochemical reaction, the electrode was washed with DI water and dried at room temperature. The morphological features were analyzed by transmission electron microscopy (TEM, FEI, Talos F200X) and energy dispersive spectroscopy (EDS). Changes in the same nanoparticle on electrochemical activation were observed by identical location transition electron microscopy (IL-TEM). The depth profile of Ir was determined using X-ray photoelectron spectroscopy (XPS) at the 4D beamline of the Pohang Accelerator Laboratory (PAL), Pohang, South Korea.

2.4. *In situ*/*operando* X-ray analysis

In situ/*operando* X-ray absorption spectroscopy (XAS) measurements were performed in fluorescence mode at the 1D beamline of the Pohang Accelerator Laboratory (PAL), Pohang, South Korea. A custom-made *in situ*/*operando* electrochemical flow cell was used to measure the catalyst during oxygen evolution. Ag/AgCl (3.5 M KCl) and Pt wire were used as the reference electrode and counter electrode, respectively. To prepare the working electrode, the catalyst ink was sprayed onto a carbon-coated Kapton film. XAS data were collected at an angle of 45° with respect to the beamline and detector. The detailed setup of *in situ*/*operando* XAS was reported in a previous paper.[28]

3. Results and discussion

Carbon supported IrNi alloy nanoparticles (denoted as IrNi/C) were prepared using the modified polyol process and used as the initial material for electrochemical activation. The morphology of the synthesized IrNi/C and the distribution of the elements were confirmed by electron microscopy. Fig. 1 and S1† show the transmission electron microscopy (TEM) images of the prepared IrNi/C. The synthesized IrNi nanoparticles have a uniform spherical shape with a size range of 10–15 nm and they are homogeneously deposited on carbon black. Based on ICP-OES analysis, the mass ratios of the elements in IrNi/C were found to be 10.3 wt% Ir and 10.6 wt% Ni. The elemental

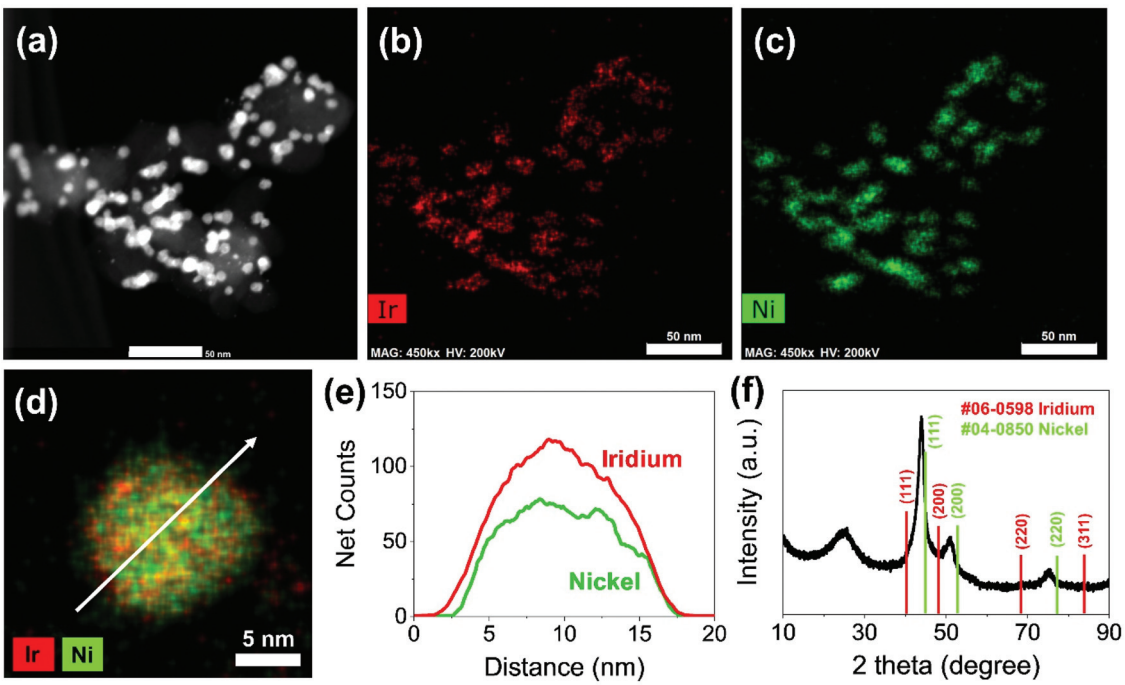

Fig. 1 Morphology of carbon supported IrNi alloy nanoparticles (IrNi/C). (a) HAADF-STEM images of pristine IrNi/C (scale bar: 50 nm). HAADF-STEM elemental mapping analysis of IrNi/C (scale bar: 50 nm): (b) red and (c) green represent Ir and Ni, respectively. (d and e) Line-scan profiles of IrNi alloy nanoparticles. (f) X-ray diffraction pattern of IrNi/C. Reference patterns are given at the bottom: JCPDS card no. 06-0598 (Ir, red) and JCPDS card no. 04-0850 (Ni, green).

distributions of Ir and Ni were also analyzed by energy dispersive X-ray (EDX) element mapping. As shown in Fig. 1b and c, Ir and Ni are homogeneously distributed, suggesting that Ir and Ni metals are well alloyed. Within one nanoparticle (Fig. 1d and e), the results of the EDS line scan of IrNi/C show that the Ir and Ni components are uniformly mixed as well. The formation of the IrNi alloy was further confirmed from X-ray diffraction (XRD) patterns (Fig. 1f). The three main diffraction patterns matched with the (111), (200), and (220) planes, showing an fcc structure.[36] The XRD peak position of IrNi/C is located between Ir (JCPDS #06-0598) and Ni (JCPDS #04-0850), which clearly confirms that IrNi/C has formed a well alloyed bimetallic structure. Fig. 2 demonstrates a morphological transformation of IrNi/C on electrochemical activation under acidic, neutral, and alkaline conditions. The electronic structure of pristine IrNi/C was activated through 50 cycles of cyclic voltammetry (CV) between 0.05 and 1.5 V *vs.* RHE at a scan rate of 500 mV s^{-1}. The activations were carried out in acid (0.05 M H_2SO_4 purged with N_2, denoted as $IrNiO_x$/C–A), neutral (0.5 M $KHCO_3$ purged with CO_2, denoted as $IrNiO_x$/C–N), and alkaline media (0.1 M KOH purged with N_2, denoted as $IrNiO_x$/C–Al) to enhance the catalytic activity. Fig. 2a, b, and S2† show the morphology changes in $IrNiO_x$/C–A by identical location TEM (IL-TEM). In previous research, it was observed that the dissolution and re-deposition of Ir occurred during fast CV scans in an acid solution, leading to the formation of amorphous IrO_x.[37,38] An Ir nanoparticle cluster was formed in the particles, whereas Ni was almost completely dissolved. This Ni-leached IrO_x structure is formed because of the unstable nature of Ni in the acid electrolyte. According to the line-scan of $IrNiO_x$/C–A (Fig. 2c), on the electrochemical activation under acid electrolyte conditions, Ni is detected only in the core of the particles, indicating that the surface Ni has dissolved, leaving behind the IrO_x shell structure. To quantify Ni dissolution during activation, the atomic composition of Ir and Ni was determined using the EDX spectrum. After the electrochemical activation under acidic conditions, the atomic ratio of Ni/Ir was changed from 3.94 to 0.097, confirming the high dissolution of Ni in the acid electrolyte. This transformation of $IrNiO_x$/C–A is consistent with the findings of a previous report.[32] Upon the activation of IrNi/C under neutral conditions, the Ni dissolution rate is greatly reduced due to its low acidity and Ni leaching occurs only in the top layer of the IrNi nanoparticles, as shown in Fig. 1d, e, and S3.† Ir is also dissolved and redeposited during this electrochemical activation, so that some of the Ir nanoparticles are deposited in the form of small particles on the carbon support. These morphological transformations can be clearly observed in the EDS line scan. A large amount of Ni is located in the core of the particle, indicating a thin Ir oxide

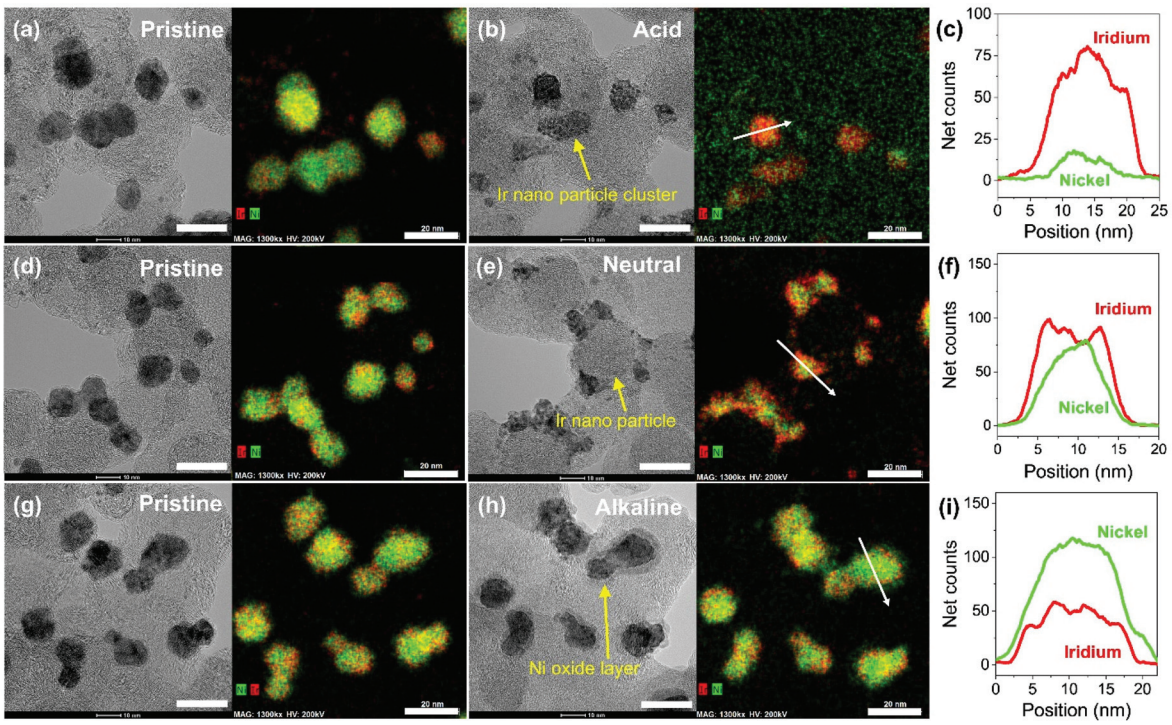

Fig. 2 Morphological transformation of electrochemically activated IrNi/C under acidic, neutral, and alkaline conditions. Identical location transmission electron microscopy (IL-TEM) images and IL-HAADF-STEM elemental mapping analysis of pristine IrNi/C before electrochemical activation under (a) acid (d) neutral and (g) alkaline conditions (scale bar: 20 nm). Identical location transmission electron microscopy (IL-TEM) images and IL-HAADF-STEM elemental mapping analysis of electrochmically activated IrNi/C under (b) acid (e) neutral and (h) alkaline conditions, which are denoted as $IrNiO_x$/C–A, $IrNiO_x$/C–N, and $IrNiO_x$/C–Al, respectively (scale bar: 20 nm). Line-scan profiles of (c) $IrNiO_x$/C–A, (f) $IrNiO_x$/C–N, and (i) $IrNiO_x$/C–Al.

shell with an IrNi core structure. According to the EDX spectrum, the Ni/Ir atomic composition of $IrNiO_x$/C–N is 3.46, suggesting that soft Ni leaching occurred during activation in neutral media. The electrochemical activation of IrNi/C under alkaline conditions tends to be different compared to that under neutral or acidic conditions. $IrNiO_x$/C–Al formed a Ni oxide layer on the particle surface, because Ni forms a passivated oxide phase without dissolution in the alkaline electrolyte according to pH-potential stability (Fig. 2g, h, S4, and S5†). The Ni/Ir atomic ratio of $IrNiO_x$/C measured using the EDX spectrum is 3.98, which is close to pristine IrNi/C (3.94), confirming no dissolution of Ni. Thus, the surface of $IrNiO_x$–Al gets oxidized during the electrochemical activation in alkaline media, leading to the Ni-rich $IrNiO_x$ shell structure of the catalyst. The EDS line-scan result also confirms the Ni-rich shell structure of $IrNiO_x$/C–Al (Fig. 2i).

To understand the changes in the electrochemical properties of IrNi/C by electrochemical activation under different pH conditions, the transformations of CV profiles (Fig. 3a–c) during electrochemical activation were observed. In all the samples, underpotentially deposited H (H_{upd}) peaks between 0.05 and 0.4 V_{RHE} disappeared during activation, stipulating the oxidation of metallic IrNi/C in all media. In the case of acid activation, the redox peak associated with the Ir(III)/Ir(VI) redox couple increased, indicating the formation of an IrO_x layer at the $IrNiO_x$/C–A surface (Fig. 3a).[39] $IrNiO_x$/C–N possessed a smaller Ir(III)/Ir(VI) redox peak area of 0.499 mC cm^{-2} than both $IrNiO_x$/C–A (0.823 mC cm^{-2}) and $IrNiO_x$/C–Al (0.773 mC cm^{-2}), signaling only a small amount of the oxide species (Fig. 3b). Furthermore, the cathodic peak position of

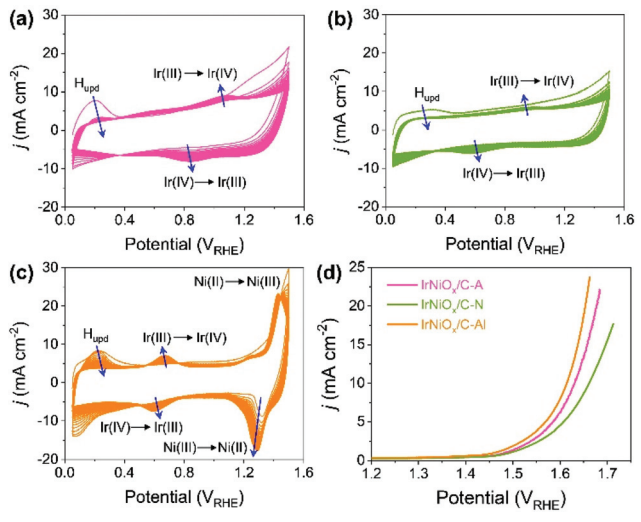

Fig. 3 Electrochemical properties of activated IrNi/C under different pH conditions. Cyclic voltammogram (CV) profiles of IrNi/C between 0.05 and 1.5 V *vs.* RHE at a scan rate of 500 mV s^{-1} in (a) acid (0.05 M H_2SO_4 purged with N_2), (b) neutral (0.5 M $KHCO_3$ purged with CO_2) and (c) alkaline media (0.1 M KOH purged with N_2). (d) *iR*-corrected LSV curves of $IrNiO_x$/C–A, $IrNiO_x$/C–N and $IrNiO_x$/C–Al in CO_2-saturated 0.5 M $KHCO_3$ at a scan rate 10 mV s^{-1}. (e) Tafel plots of $IrNiO_x$/C–A, $IrNiO_x$/C–N, and $IrNiO_x$/C–Al.

$IrNiO_x$/C–N is located at 0.65 V_{RHE}, which is lower than that of $IrNiO_x$/C–A. In a previous report, it was expounded that the lower cathodic peak position of Ir represents the reduction of IrO_2 and not IrO_x with a high oxidation state.[37,38] This implies that the electrochemical activation under neutral conditions slightly oxidizes the Ir surface to IrO_x. $IrNiO_x$/C–Al shows CV shapes different from both $IrNiO_x$/C–A and $IrNiO_x$/C–N. The redox peak associated with Ir(III)/Ir(VI) is located between 0.6 and 0.7 V_{RHE} under alkaline conditions (Fig. 3c). The large Ni(II)/Ni(III) redox peak with an area of 2.086 mC cm^{-2} is observed at 1.2–1.3 V_{RHE}, indicating the abundant Ni oxide of $IrNiO_x$/C–Al.[40,41] The above observations are in good agreement with the HR-TEM results.

The effects of the electrochemical activation in different media for OER catalytic activity were evaluated by linear sweep voltammetry (LSV) in CO_2 saturated 0.5 M $KHCO_3$ solution with a scan rate of 10 mV s^{-1} and a rotating speed of 1600 rpm. As presented in Fig. 3d, the LSV of $IrNiO_x$/C–Al exhibited an anodic current onset at approximately 1.4 V_{RHE}, which was 50 mV lower than that of $IrNiO_x$/C–A and $IrNiO_x$/C–N. Moreover, the overpotential at a current density of 10 mA cm^{-2} of $IrNiO_x$/C–Al was only 384 mV, which was lower than that of $IrNiO_x$/C–A (400 mV) and $IrNiO_x$/C–N (431 mV). The enhanced OER activity in neutral media is compared with those previously reported as shown in Table S1.† These results suggest that $IrNiO_x$/C–Al and $IrNiO_x$/C–A possess higher OER catalytic activity than $IrNiO_x$/C–N. Moreover, the observations reveal that despite using the same starting catalyst, different electrochemical activations can result in different catalytic activities. The electrochemical stability of the prepared catalysts was tested at 10 mA cm^{-2} constant water oxidation current density for 10 h in CO_2 saturated 0.5 M $KHCO_3$ solution and the results are shown in Fig. S6.† $IrNiO_x$/C–N shows the gradually increased potentials, which indicate slow catalytic degradation. On the other hand, $IrNiO_x$/C–A and $IrNiO_x$/C–Al show stable behavior for 10 h in CO_2 saturated 0.5 M $KHCO_3$. These results indicate that $IrNiO_x$/C–Al, which is electrochemically activated under alkaline conditions, is more efficient and durable than catalysts activated under acidic and neutral conditions.

To validate in detail the electronic structure of the electrochemically treated IrNi/C in different media, depth-profiled X-ray photoelectron spectroscopy (XPS) was performed with 210 eV and 550 eV kinetic energies (KE) at the 4D beamline of the Pohang Accelerator Laboratory (PAL). The deconvolution of the Ir 4f spectra yielded three components: Ir^0 (metallic Ir, 60.9 and 63.9 eV), Ir^{VI} (rutile Ir oxide, 61.8 and 64.8 eV), and Ir^{III} (amorphous Ir oxide, 62.3 and 65.3 eV). In Fig. 4a, the Ir 4f region of pristine IrNi/C indicates a mostly metallic state. The two dominant peaks for all electrochemically activated IrNi/C are located between the Ir^{VI} and Ir^{III} species binding energy, denoting the oxidation states of the Ir species (Fig. 4b–d). The Ir 4f peak at 210 eV is more oxidized than that at KE 550 eV, confirming that IrNi/C was oxidized from the surface by electrochemical activation. Based on the XPS fitting at KE 210 eV, the Ir^{III} species ratio was found to be 58.0% for $IrNiO_x$/C–A and 66.6% for $IrNiO_x$/C–Al. This shows that the surface of IrNi/

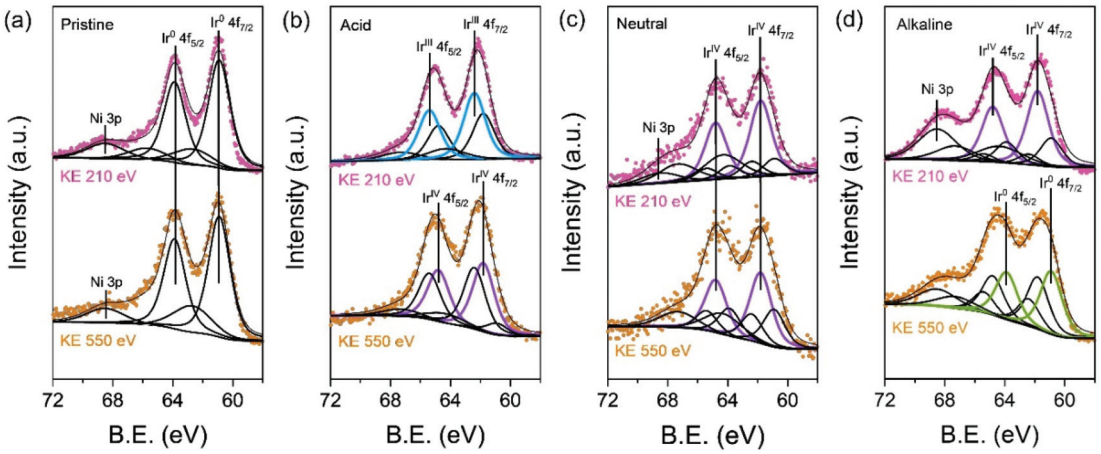

Fig. 4 Electronic structures of electrochemically activated IrNi/C under acidic, neutral, and alkaline conditions. High-resolution XPS spectra for Ir 4f of (a) pristine IrNi/C, (b) $IrNiO_x$/C–A, (c) $IrNiO_x$/C–N, and (d) $IrNiO_x$/C–Al at kinetic energies of 210 eV and 550 eV.

C is converted to IrO_x species by CV in acidic and alkaline media. The Ni peaks of $IrNiO_x$/C–Al are located at 856 eV and are assigned to the binding energy of $Ni(OH)_2$. This demonstrates that not only Ir, but also Ni is oxidized by the alkaline electrochemical activation (Fig. S7†). In contrast, $IrNiO_x$/C–N exhibited 62.3% Ir^{VI} species component, signaling an Ir oxide layer with a small amount of IrO_x. This observation implies that neutral conditions do not favor the oxidation of the catalyst surface, which is in agreement with the CV results. A similar observation is also found in the *ex situ* X-ray adsorption

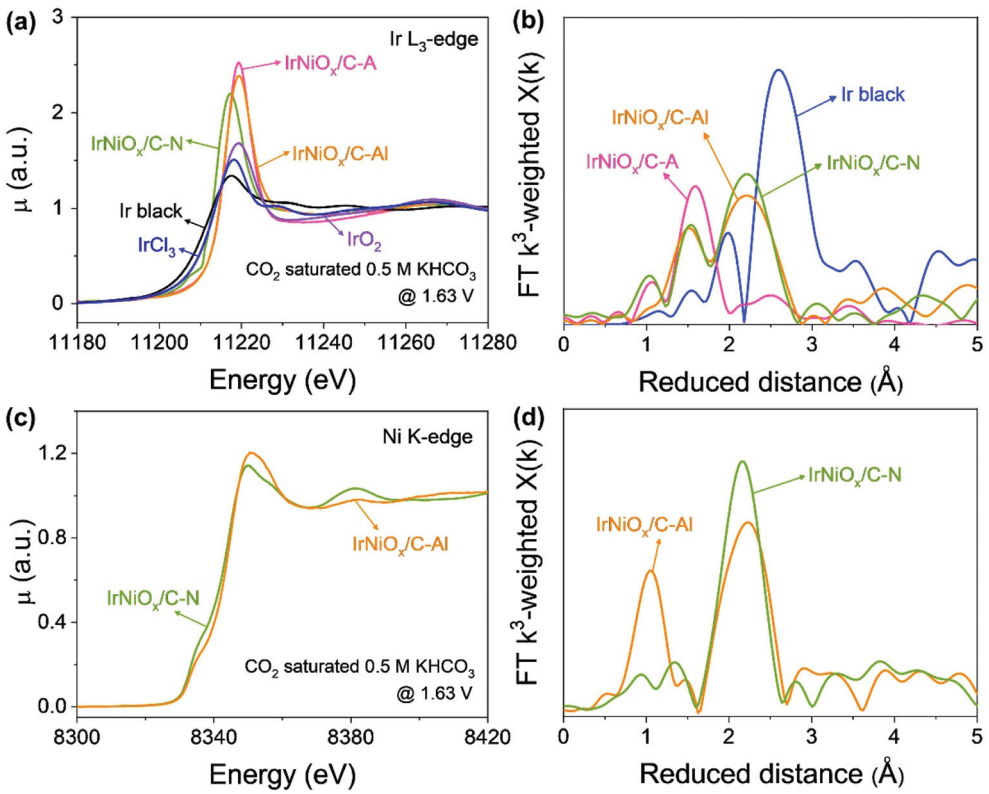

Fig. 5 *In situ*/*operando* X-ray absorption spectroscopy (XAS) study under OER conditions in CO_2-saturated 0.5 M $KHCO_3$. (a) Ir L_3-edge XANES region of $IrNiO_x$/C–A, $IrNiO_x$/C–N, and $IrNiO_x$/C–Al at 1.63 V_{RHE} in CO_2 saturated 0.5 M $KHCO_3$. Ir foil, $IrCl_3$, and IrO_2 as references were measured under *ex situ* conditions. (b) k^3-Weighted Fourier transforms of EXAFS profiles collected at the Ir L_3-edge of $IrNiO_x$/C–A, $IrNiO_x$/C–N and $IrNiO_x$/C–Al. (c) Ni K-edge XANES region of $IrNiO_x$/C–N and $IrNiO_x$/C–Al at 1.63 V_{RHE} in CO_2 saturated 0.5 M $KHCO_3$. (d) k^3-Weighted Fourier transforms of EXAFS profiles collected at the Ni K-edge of $IrNiO_x$/C–N and $IrNiO_x$/C–Al.

fine spectrum (XAFS). In Fig. S8,† the X-ray adsorption near edge structure (XANES) spectra and extended X-ray adsorption fine structure (EXAFS) spectra of the activated samples indicate that $IrNiO_x$/C–A and $IrNiO_x$/C–Al show higher oxidation states than $IrNiO_x$/C–N.

To gain insight into the catalytic activity enhancement by electrochemical activation, the *in situ*/*operando* XAFS of the Ir L_3-edge and Ni K-edge was carried out at the 1D KIST-PAL beamline of the Pohang Accelerator Laboratory. Customized electrochemical flow cells were used for the *in situ*/*operando* XAFS measurements. Fig. 5 shows that *operando* XAFS measurements were conducted during the OER under neutral conditions after electrochemical activation under different pH conditions. At the Ir L_3-edge, the XANES spectra of $IrNiO_x$/C–A and $IrNiO_x$/C–Al showed a highly identical white line position, whereas that of $IrNiO_x$/C–N exhibited a negatively shifted white line position, suggesting that $IrNiO_x$/C–A and $IrNiO_x$/C–Al possess a higher number of d-band holes than $IrNiO_x$/C–N under OER conditions (Fig. 5a). The area of the white line peak of $IrNiO_x$/C–A (21.03) was larger than that of $IrNiO_x$/C–Al (19.80), indicating that the oxide thickness in the case of $IrNiO_x$/C–A is more than that of $IrNiO_x$/C–Al (Fig. S9†). This is further proved by the EXAFS results in Fig. 5b. The distance of Ir–M is reduced in the IrNi/C sample to be shorter than that of Ir black, confirming the existence of the IrNi alloyed structure. The Ir–O peaks of $IrNiO_x$/C–A indicate fully oxidized $IrNiO_x$ nanoparticles, whereas the remaining Ir–M peaks of $IrNiO_x$/C–Al represent the unoxidized core of the $IrNiO_x$/C–Al nanoparticle during the OER. We expect that the thick Ni-rich $IrNiO_x$ layer of $IrNiO_x$/C–Al observed by HR-TEM would inhibit the oxidation of the nanoparticle core. Strasser *et al.* reported that a higher number of d-band holes of Ir increase the hole character of the oxygen ligands, enhancing their electrophilic character.[32] This promotes the nucleophilic attack of water molecules, thus reducing the kinetic barrier of the OER. $IrNiO_x$/C–A and $IrNiO_x$/C–Al possess more number of d-band holes under OER conditions than $IrNiO_x$/C–N, indicating the greater OER activity of $IrNiO_x$/C–A and $IrNiO_x$/C–Al. In Fig. 5c, $IrNiO_x$/C–Al reveals higher Ni XANES peak positions and areas than both $IrNiO_x$/C–N and *ex situ* $IrNiO_x$/C–Al in the OER under neutral conditions, indicating that the Ni in $IrNiO_x$/C–Al has a higher oxidation state in the OER. This is also observed in the Ni-EXAFS peaks (Fig. 5d). An increased Ni–O bond peak is observed, indicating the existence of an oxide layer of $IrNiO_x$/C–Al in the OER. In previous studies, high-valent Ni species of Ni-based catalysts were observed in the OER and are expected to act as active sites.[42,43] The formation of higher oxidation states of nickel such as Ni^{IV} improves the OER catalytic activity under neutral conditions.[44] Thus, Ni in $IrNiO_x$/C–Al can be a good active site for the OER in neutral media. The above results reveal that $IrNiO_x$/C–Al possesses a Ni-rich $IrNiO_x$ layer, with a configuration including IrO_x active sites with a high number of d-band holes and NiO_x active sites with a high oxidation state under OER conditions. This configuration of the two active species synergistically enhances the OER catalytic activity of $IrNiO_x$/C–Al in neutral media.

4. Conclusions

In summary, we have identified the effects of the electrochemical activation of IrNi nanoparticles under different pH conditions and evaluated the OER activity under neutral conditions applicable to CO_2RR systems. $IrNiO_x$/C–A activated under acidic conditions exhibits a Ni-leached IrNi@IrO_x structure and $IrNiO_x$/C–Al activated under alkaline conditions has a Ni-rich IrNi@$IrNiO_x$ structure. Meanwhile, $IrNiO_x$/C–N activated under neutral conditions possesses a lower oxidized, thin Ir oxide shell structure. *In situ*/*operando* XAS demonstrates that the Ni-rich $IrNiO_x$ surface of $IrNiO_x$/C–Al has an IrO_x active site with a high number of d-band holes and a NiO_x active site with a high oxidation state during the OER, leading to superior OER catalytic activity with an overpotential of 384 mV at 10 mA cm^{-2} under neutral conditions. These observations are also confirmed by synchrotron-based XPS depth profiling measurements. Our research suggests that the intrinsic properties of the catalyst change with the environment of the electrochemical activation, and that the catalyst structure suitable for the electrochemical reaction can be adjusted through the applied electricity and pH conditions.

Conflicts of interest

There are no conflicts to declare.

Acknowledgements

This work was supported by the Korea Institute of Science and Technology (KIST) institutional program and partially supported by the National Research Foundation of Korea (NRF) grant funded by the Korea Government (MEST) (No. 2019R1A2C2005521). We acknowledge the Advanced Analysis Center at KIST for the TEM, XPS and ICP-MS measurements. We acknowledge 1D XRS KIST-PAL and 4D beamline of PAL for the XAS and XPS measurements, respectively.

References

1 S. Chu, Y. Cui and N. Liu, *Nat. Mater.*, 2017, **16**, 16–22.
2 N.-T. Suen, S.-F. Hung, Q. Quan, N. Zhang, Y.-J. Xu and H. M. Chen, *Chem. Soc. Rev.*, 2017, **46**, 337–365.
3 S. Ghosh and R. N. Basu, *Nanoscale*, 2018, **10**, 11241–11280.
4 S. Ma and P. J. Kenis, *Curr. Opin. Chem. Eng.*, 2013, **2**, 191–199.
5 N. S. Spinner, J. A. Vega and W. E. Mustain, *Catal. Sci. Technol.*, 2012, **2**, 19–28.
6 Y. Li and Q. Sun, *Adv. Energy Mater.*, 2016, **6**, 1600463.
7 B. Zhang, Y. H. Lui, L. Zhou, X. Tang and S. Hu, *J. Mater. Chem. A*, 2017, **5**, 13329–13335.
8 Y. Dong, S. Komarneni, N. Wang, W. Hu and W. Huang, *J. Mater. Chem. A*, 2019, **7**, 6995–7005.

9 L. Cui, D. Liu, S. Hao, F. Qu, G. Du, J. Liu, A. M. Asiri and X. Sun, *Nanoscale*, 2017, **9**, 3752–3756.
10 L. Fu, X. Hu, Y. Li, G. Cheng and W. Luo, *Nanoscale*, 2019, **11**, 8898–8905.
11 M. Vuković, *J. Appl. Electrochem.*, 1987, **17**, 737–745.
12 A. Grimaud, A. Demortière, M. Saubanère, W. Dachraoui, M. Duchamp, M.-L. Doublet and J.-M. Tarascon, *Nat. Energy*, 2016, **2**, 1–10.
13 W. H. Lee and H. Kim, *Catal. Commun.*, 2011, **12**, 408–411.
14 Y. Zhao, M. Luo, S. Chu, M. Peng, B. Liu, Q. Wu, P. Liu, F. M. de Groot and Y. Tan, *Nano Energy*, 2019, **59**, 146–153.
15 L. Fu, F. Yang, G. Cheng and W. Luo, *Nanoscale*, 2018, **10**, 1892–1897.
16 P. Jovanovič, N. Hodnik, F. Ruiz-Zepeda, I. Arčon, B. Jozinović, M. Zorko, M. Bele, M. Šala, V. S. Šelih and S. Hočevar, *J. Am. Chem. Soc.*, 2017, **139**, 12837–12846.
17 V. Pfeifer, T. E. Jones, J. J. Velasco Vélez, C. Massué, R. Arrigo, D. Teschner, F. Girgsdies, M. Scherzer, M. T. Greiner and J. Allan, *Surf. Interface Anal.*, 2016, **48**, 261–273.
18 V. Pfeifer, T. Jones, J. V. Vélez, C. Massué, M. Greiner, R. Arrigo, D. Teschner, F. Girgsdies, M. Scherzer and J. Allan, *Phys. Chem. Chem. Phys.*, 2016, **18**, 2292–2296.
19 V. Pfeifer, T. E. Jones, J. J. V. Vélez, R. Arrigo, S. Piccinin, M. Hävecker, A. Knop-Gericke and R. Schlögl, *Chem. Sci.*, 2017, **8**, 2143–2149.
20 C. Massué, V. Pfeifer, M. van Gastel, J. Noack, G. Algara-Siller, S. Cap and R. Schlögl, *ChemSusChem*, 2017, **10**, 4786–4798.
21 S.-A. Park, K.-S. Kim and Y.-T. Kim, *ACS Energy Lett.*, 2018, **3**, 1110–1115.
22 M. Tariq, W. Q. Zaman, W. Sun, Z. Zhou, Y. Wu, L.-m. Cao and J. Yang, *ACS Sustainable Chem. Eng.*, 2018, **6**, 4854–4862.
23 J. Feng, F. Lv, W. Zhang, P. Li, K. Wang, C. Yang, B. Wang, Y. Yang, J. Zhou and F. Lin, *Adv. Mater.*, 2017, **29**, 1703798.
24 Y. Pi, Q. Shao, P. Wang, J. Guo and X. Huang, *Adv. Funct. Mater.*, 2017, **27**, 1700886.
25 H. N. Nong, H. S. Oh, T. Reier, E. Willinger, M. G. Willinger, V. Petkov, D. Teschner and P. Strasser, *Angew. Chem., Int. Ed.*, 2015, **54**, 2975–2979.
26 C. Wang, Y. Sui, G. Xiao, X. Yang, Y. Wei, G. Zou and B. Zou, *J. Mater. Chem. A*, 2015, **3**, 19669–19673.
27 Q. Wang, X. Huang, Z. L. Zhao, M. Wang, B. Xiang, J. Li, Z. Feng, H. Xu and M. Gu, *J. Am. Chem. Soc.*, 2020, **142**(16), 7425–7433.
28 W. H. Lee, H. N. Nong, C. H. Choi, K. H. Chae, Y. J. Hwang, B. K. Min, P. Strasser and H.-S. Oh, *Appl. Catal., B*, 2020, 118820.
29 T. Reier, Z. Pawolek, S. Cherevko, M. Bruns, T. Jones, D. Teschner, S. r. Selve, A. Bergmann, H. N. Nong and R. Schlögl, *J. Am. Chem. Soc.*, 2015, **137**, 13031–13040.
30 G. Meng, W. Sun, A. A. Mon, X. Wu, L. Xia, A. Han, Y. Wang, Z. Zhuang, J. Liu and D. Wang, *Adv. Mater.*, 2019, **31**, 1903616.
31 L. C. Seitz, C. F. Dickens, K. Nishio, Y. Hikita, J. Montoya, A. Doyle, C. Kirk, A. Vojvodic, H. Y. Hwang and J. K. Norskov, *Science*, 2016, **353**, 1011–1014.
32 H. N. Nong, T. Reier, H.-S. Oh, M. Gliech, P. Paciok, T. H. T. Vu, D. Teschner, M. Heggen, V. Petkov and R. Schlögl, *Nat. Catal.*, 2018, **1**, 841–851.
33 S. Rudi, D. Teschner, V. Beermann, W. Hetaba, L. Gan, C. Cui, M. Gliech, R. Schlögl and P. Strasser, *ACS Catal.*, 2017, **7**, 6376–6384.
34 X. Chia, A. Ambrosi, D. Sedmidubský, Z. Sofer and M. Pumera, *Chem. – Eur. J.*, 2014, **20**, 17426–17432.
35 R. M. Arán-Ais, J. Solla-Gullón, M. Gocyla, M. Heggen, R. E. Dunin-Borkowski, P. Strasser, E. Herrero and J. M. Feliu, *Nano Energy*, 2016, **27**, 390–401.
36 W. Wu, Z. Chen, X. Lin, B. Li and X. Cong, *Vacuum*, 2011, **86**, 429–437.
37 S. Cherevko, S. Geiger, O. Kasian, A. Mingers and K. J. Mayrhofer, *J. Electroanal. Chem.*, 2016, **773**, 69–78.
38 S. Cherevko, S. Geiger, O. Kasian, A. Mingers and K. J. Mayrhofer, *J. Electroanal. Chem.*, 2016, **774**, 102–110.
39 H.-S. Oh, H. N. Nong, T. Reier, M. Gliech and P. Strasser, *Chem. Sci.*, 2015, **6**, 3321–3328.
40 C. Tang, H. S. Wang, H. F. Wang, Q. Zhang, G. L. Tian, J. Q. Nie and F. Wei, *Adv. Mater.*, 2015, **27**, 4516–4522.
41 S. Klaus, Y. Cai, M. W. Louie, L. Trotochaud and A. T. Bell, *J. Phys. Chem. C*, 2015, **119**, 7243–7254.
42 M. Görlin, J. Ferreira de Araújo, H. Schmies, D. Bernsmeier, S. r. Dresp, M. Gliech, Z. Jusys, P. Chernev, R. Kraehnert and H. Dau, *J. Am. Chem. Soc.*, 2017, **139**, 2070–2082.
43 J. Yan, L. Kong, Y. Ji, J. White, Y. Li, J. Zhang, P. An, S. Liu, S.-T. Lee and T. Ma, *Nat. Commun.*, 2019, **10**, 1–10.
44 X. Zheng, B. Zhang, P. De Luna, Y. Liang, R. Comin, O. Voznyy, L. Han, F. P. G. de Arquer, M. Liu and C. T. Dinh, *Nat. Chem.*, 2018, **10**, 149.